Exoplanet detection in angular and spectral differential imaging with an accelerated proximal gradient algorithm

Nicolas Mil-Homens Cavaco*, Laurent Jacques and P.-A. Absil

UCLouvain - ICTEAM institute
B-1348 Louvain-la-Neuve - Belgium

Abstract. Differential imaging is a technique to post-process images captured by ground-based telescopes during an observation campaign, in order to make exoplanets in a distant planetary system directly visible and to remove the so-called quasi-static speckles that dramatically affect detection capabilities. In order to introduce geometric diversity between the exoplanets and the quasi-static speckles, the light is split into spectral channels during the data acquisition process, producing a 4-D data cube with images recorded at many wavelengths and at many times. In this work, we propose to follow an inverse problem approach to model the astronomical data as the contribution of a low-rank component containing the background of quasi-static speckles and a sparse component containing the exoplanets. We then formulate the resulting model as a convex non-smooth optimization model so that an accelerated proximal gradient descent can be used to solve the detection problem.

1 Introduction

Direct imaging of exoplanets yields useful information to astronomers willing to study their properties, such as orbital trajectories from which important characteristics can be deduced (*e.g.*, orbital period, mass). However, imaging these exoplanets remains a challenging task; it requires both specific observation strategies and dedicated post-processing techniques to detect the tiny amount of starlight emitted by exoplanets. Since specific noises make it impossible to detect exoplanets on a single image, astronomers have devised acquisition techniques to observe a given exoplanet under various speckle alterations. This principle supports angular differential imaging (ADI), spectral differential imaging (SDI), or a combination of both (ASDI) [7]. For instance, ADI leverages the Earth rotation during one observation campaign to detect a rotating exoplanet (in the Earth coordinate frame) while the nature of the speckle (atmospheric or instrumental) makes it fixed. In SDI, observation diversity is achieved through wavelength variations: the spatial configuration of the exoplanets (before the instrumental PSF) is constant while the speckles and the instrument PSF are dilated by a wavelength-dependent factor. By exploiting this variety between exoplanets and speckles, several advanced post-processing algorithms in ADI have been proposed to unmix both components. Among them, a first family of

*Research Fellow of the Fonds de la Recherche Scientifique - FNRS.

methods models the background (capturing the speckle and the starlight residual) as a low-rank matrix, then subtracts the background from the images to finally derotates and average the residual images to reveal the exoplanets. The simplest method is the PCA subtraction technique (also called KLIP [13]) that obtains the background by computing a trunctated SVD accross the time and the spatial domain. Subsequently, [8, 12, 14] added to the low-rank model a sparse component capturing the exoplanet signal to lower the self-subtraction effect of the planetary signal induced by PCA. On the other hand, another background model approach named PACO (for patch covariance) instead learns a statistical model of the background from the data by looking at the local spatial covariance between pixels in the images [6]. From the work of [3, 10] leveraging PCA and [6] adopting PACO, it was shown that including SDI data into ADI allows to reach a better contrast between an exoplanet and its host star on the post-processed images. In this context, we propose to enhance the PCA algorithm applied to ASDI data by introducing a sparse component modeling the exoplanets, and hence extending the work of [14] to ASDI. Moreover, we compare the performance of the new ASDI algorithm with the classical PCA algorithm by drawing a modified version of the so-called Receiver Operating Characteristic curves.

2 Low-rank plus sparse model for ASDI data cubes

Preprocessing: Starting from an ASDI data cube $Y \in \mathbb{R}^{WT \times N^2}$ of $N \times N$ images captured at W wavelengths $\lambda_1 < \ldots < \lambda_W$ and T times, we would like to reconstruct a map $S \in \mathbb{R}^{W \times N^2}$ containing the exoplanets, which have a flux varying with the wavelength. Similarly to [3, 10], to freeze the speckle pattern along the spectral dimension, which is the key ingredient for having a low-rank quasi-static speckle background, we preprocess the data cube Y by scaling each image, captured at a given wavelength $\lambda \in \{\lambda_\ell\}_{\ell=1}^W$, with respect to the scale factor λ_W/λ, yielding a data cube of $n \times n$ images, where $n = N\lceil \frac{\lambda_W}{\lambda_1} \rceil > N$.[1] Moreover, an annular mask of inner radius R_{in} and outer radius R_{out} is applied on the scaled data cube using the mask operator $\mathcal{P}_\Omega : \mathbb{R}^{WT \times n^2} \mapsto \mathbb{R}^{WT \times |\Omega|}$ that only keeps the columns indexed by the annular mask $\Omega \subseteq \{1, \ldots, n^2\}$. Scaling and masking the data cube $Y \in \mathbb{R}^{WT \times N^2}$ provides the preprocessed ASDI data cube $Z \in \mathbb{R}^{WT \times |\Omega|}$, which can be decomposed into three additive terms: the speckle pattern (low-rank), the planetary signal (sparse) and the detector noise (assumed to be Gaussian).

The sparse component: Since the number of exoplanets in the cube is finite and much lower than N^2, we expect that $S \in \mathbb{R}^{W \times N^2}$, containing the exoplanets, will be sparse according to the spatial dimension. Moreover, if an exoplanet lies in the preprocessed data cube Z, then it will be a point source convolved with the non-coronagraphic point spread function (PSF) of the telescope[2] and that rotates according to the parallactic angle due to the Earth's rotation in ADI. Combining

[1] To be more precise, we first apply a zero-padding of $\frac{1}{2}(n-N)$ at each border of the images before scaling them. This prevents data from leaving the image during scaling.

[2] Assuming a sufficiently large angular separation of the exoplanets so that coronagraph effects become negligible.

the rotation (involving an interpolation of the pixel grid) with the convolution and applying the scaling and the mask operators coming from preprocessing (see Figure 1), we obtain what we call the trajectorlet operator $\Psi(\cdot)$ (inspired by [14]) modeling the behavior of the planetary component in the data cube: $\Psi : \mathbb{R}^{W\times N^2} \mapsto \mathbb{R}^{WT\times|\Omega|} : S \to \Psi(S) := \mathcal{P}_\Omega \mathcal{Q}\mathcal{D}\mathcal{T}(S)$.

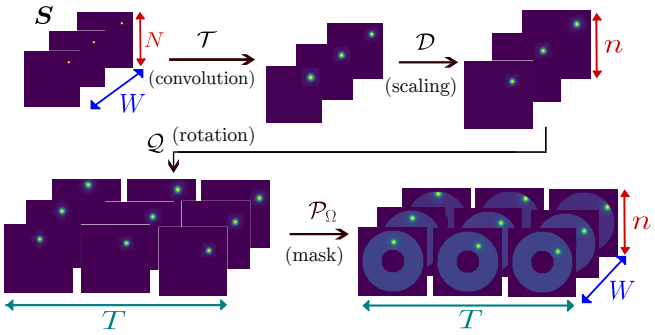

Fig. 1: Illustration of the trajectorlet operator

The low-rank component: Thanks to the preprocessing step freezing the background along the spectral axis, we can model it as a low-rank matrix $L = U_r X^\top$, where $U_r \in \mathbb{R}^{WT\times r}$ contains the r first left singular vectors of the preprocessed ASDI data cube Z, assuming that the low-rankness of speckles is not impacted by faint exoplanets, while $X \in \mathbb{R}^{|\Omega|\times r}$ is a matrix of parameters that is to be optimized.

The inverse problem: Combining the previous considerations, this leads us to the following convex non-smooth optimization problem:

$$\min_{X\in\mathbb{R}^{r\times|\Omega|}, S\in\mathbb{R}^{W\times N^2}} \frac{1}{2}\|Z - U_r X^\top - \Psi(S)\|_F^2 + \alpha \sum_{j=1}^{N^2} \|S_j\|_2 \qquad \alpha > 0, \quad (1)$$

where $U_r X^\top$ models the background, $\Psi(S)$ models the exoplanets and, $S_j \in \mathbb{R}^W$ are the columns of S. We solve (1) via an accelerated version of the proximal gradient descent, named FISTA [1], with the (columnwise) $\ell_{2,1}$ mixed-norm proximity operator [2, 9] to manage the convex non-smooth regularization term. Our implementation is fully compatible with PyTorch so that one can use automatic differentiation to obtain the gradient of the fidelity term (including the interpolations used in Ψ) in the objective function.[3]

Initialization: To initialize FISTA, we set all the entries of $S^{(0)}$ to zero, while $X^{(0)}$ is defined via the truncated SVD of Z, *i.e.*, $(X^{(0)})^\top := \Sigma_r V_r^\top$ such that $U_r \Sigma_r V_r^\top := \mathrm{SVD}_r(Z)$.

3 Performance assessment

Detection procedure: Considering a threshold $\tau > 0$, any ASDI algorithm provides a detection map $M \in \mathbb{R}^{N\times N}$ such that $M_{ij} > \tau$ means that an exo-

[3]Code available at `https://github.com/mhd1900/fista_asdi`.

planet is predicted at location (i, j), for some $i, j \in \{1, \dots, N\}$. For instance, for model (1), we define M as the spatial map of the average planetary spectra $\frac{1}{W} 1_W^\top S$ reshaped into an $N \times N$ image, while in PCA we use the so-called SNR detection map relying on a two-sample t-test [11]. To compare the performance of several ASDI algorithms, we generate Receiver Operating Characteristic (ROC) curves similar to [5]. For a collection of data cubes free of exoplanets, we inject in each of them one single artificial exoplanet (using the VIP toolbox [4]) successively at the center of each ball shown in Figure 2. These balls have a diameter equal to the mean aperture $\bar{\lambda}/D$ and are located at a distance of $4\bar{\lambda}/D, 5\bar{\lambda}/D, 6\bar{\lambda}/D$ from the center of the image.

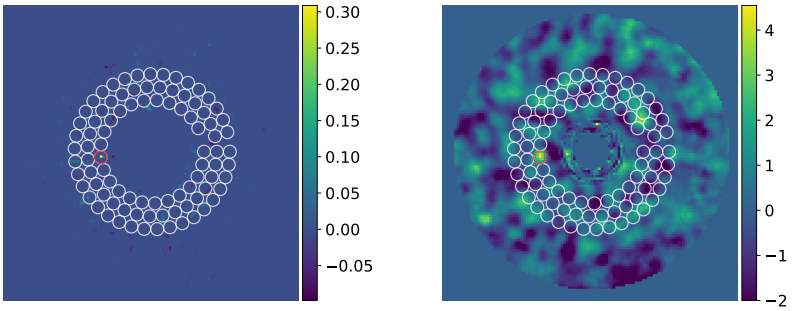

Fig. 2: Example of a detection map provided by the solution of model (1) (left) and the PCA algorithm (right). The red ball contains the injected exoplanet.

For each ball in the detection map, we predict that it contains an exoplanet if at least one pixel inside the ball is above the threshold $\tau > 0$. Following this procedure, we count the numbers of True Positives, False Positives, False Negatives and True Negatives (TP, FP, FN and TN) at a given τ for each data cube and sum up these TP, FP, FN, TN over all the data cubes to draw the ROC curves. An advantage of this procedure is that injecting planets with zero flux will lead to exactly diagonal ROC curves as stated in Theorem 3.1, which means that any algorithm has no a priori advantage over the others.

Theorem 3.1. *Consider m data cubes and m balls, where a single exoplanet is injected with zero flux at the center of a different ball for each data cube. Then, $TPR = FPR$ for any detection map M and for any threshold τ.*

Proof. See Appendix A. □

Numerical experiments: We compare the performance of model (1) solved using FISTA with the PCA algorithm applied on a version free of exoplanets of the data cube `sphere_ifs_cube_2` from phase 1 of the EIDC.[4] It is composed of 112 images divided into 39 spectral channels. We subsample the data cube by selecting temporal images and spectral channels at regular intervals so that $W = 10$ and $T = 52$, and we reduce the size of images to $N = 120$ to lower the memory and time complexities. The rank is fixed to $r = 30$ for PCA and $r = 40$

[4] `https://exoplanet-imaging-challenge.github.io`.

for model (1) as it was observed to perform the best among the tested values $r \in \{20, 30, 40, 50\}$. Regarding the sparsity level, we compare $\alpha = 0$ with $\alpha = 2$. Finally, the parameters of the annular mask Ω are set to $R_{\text{in}} = 5\bar{\lambda}/D$ and $R_{\text{out}} = 12\bar{\lambda}/D$ to make model (1) valid inside that mask. To draw the ROC curves, we generate a collection of 92 data cubes containing a single exoplanet injected in one of the 92 balls of Figure 2 with a flux of $c \cdot \sigma_{\text{ann}}(\lambda)$, where $c \in \{0, 0.25, 0.5\}$ and $\sigma_{\text{ann}}(\lambda)$ is the spatiotemporal standard deviation of the background in an annulus of $2\bar{\lambda}/D$ centered at the location of the injected exoplanet [5, 14]. In Figure 3, we observe that a zero sparsity level leads to a poor TPR for any level of injected flux $c > 0$. On the other hand, at $\alpha = 2$, the new algorithm consistently draws a better ROC curve and reaches a better TPR at FPR $= 0$ for both $c = 0.25$ and $c = 0.5$ compared to PCA.

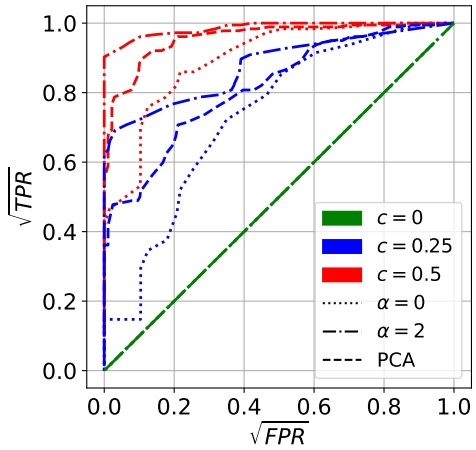

Fig. 3: ROC curves based on the SNR detection map for PCA and the average spectrum for model (1) with two sparsity levels $\alpha \in \{0, 2\}$. Colors correspond to different levels of injected flux while the line style refer to a specific algorithm.

4 Conclusion and future works

In this work, we have investigated an extention of the model-based method for exoplanet detection proposed in [14] to manage both ADI and SDI data, by adopting a convex version of both the low-rank and the sparse constraints to use FISTA as optimization algorithm. In future research, we will investigate how we can avoid interpolation of the pixel grid induced by both the rotation and the scaling operators.

A Appendix

Proof of theorem 3.1: Let $E, C \in \{0, 1\}^{m \times m}$ be two matrices such that $E_{ij} = 1$ if there is an injection at ball j in data cube i and 0 otherwise, and $C_{ij} = 1$ if there is a prediction at ball j in detection map i and 0 otherwise. Without loss of generality, notice that $E = \text{Id}$. Since injected planets

have zero flux, any ASDI algorithm keeps returning the same detection map, which means that $\exists c \in \{0,1\}^m$ such that $C = \mathbf{1}c^\top$. By construction, we have $\mathrm{P} = m$, $\mathrm{N} = (\mathrm{N}+\mathrm{P}) - \mathrm{P} = m^2 - m$, $\mathrm{TP} = \sum_{i,j=1}^{m} C_{ij}E_{ij} = \mathrm{tr}(C) = \mathbf{1}^\top c$ and $\mathrm{FP} = \sum_{i,j=1}^{m} C_{ij}(1-E_{ij}) = \mathbf{1}^\top C\mathbf{1} - \mathbf{1}^\top c = (m-1)\mathbf{1}^\top c$. Hence, $\mathrm{FPR} = \frac{\mathrm{FP}}{\mathrm{N}} = \frac{(m-1)\mathbf{1}^\top c}{m^2-m} = \frac{\mathbf{1}^\top c}{m} = \frac{\mathrm{TP}}{\mathrm{P}} = \mathrm{TPR}$.

Acknowledgements: This work was supported by the FNRS under Grant no T.0001.23. It has made use of the Exoplanet Imaging Data Challenge, collaboratively managed and maintained by members of the high-contrast imaging community, mainly led at IPAG/CNRS/UGA (Grenoble, France) and PSILab/STAR institute/ULiège (Liège, Belgium). Computational resources have been provided by the Consortium des Équipements de Calcul Intensif (CÉCI), funded by the Fonds de la Recherche Scientifique de Belgique (F.R.S.-FNRS) under Grant no 2.5020.11 and by the Walloon Region.

References

[1] A. Beck and M. Teboulle. A fast iterative shrinkage-thresholding algorithm with application to wavelet-based image deblurring. In *2009 IEEE International Conference on Acoustics, Speech and Signal Processing*, pages 693–696, 2009. ISSN: 2379-190X.

[2] G. Chierchia et al. The proximity operator repository. *User's guide http://proximity-operator.net/download/guide.pdf*, 2020.

[3] V. Christiaens et al. Separating extended disc features from the protoplanet in PDS 70 using VLT/SINFONI. *Monthly Notices of the Royal Astronomical Society*, 486(4):5819–5837, 2019.

[4] V. Christiaens et al. VIP: A python package for high-contrast imaging. *Journal of Open Source Software*, 8(81):4774, 2023.

[5] H. Daglayan et al. Likelihood ratio map for direct exoplanet detection. In *2022 IEEE 5th International Conference on Image Processing Applications and Systems (IPAS)*, volume Five, pages 1–5, 2022.

[6] O. Flasseur et al. PACO ASDI: an algorithm for exoplanet detection and characterization in direct imaging with integral field spectrographs. *A&A*, 637:A9, 2020.

[7] K. B. Follette. An introduction to high contrast differential imaging of exoplanets and disks. *Publications of the Astronomical Society of the Pacific*, 135(1051):093001, 2023.

[8] C. A. Gomez Gonzalez et al. Low-rank plus sparse decomposition for exoplanet detection in direct-imaging ADI sequences: The LLSG algorithm. *A&A*, 589:A54, 2016.

[9] A. Gramfort et al. Mixed-norm estimates for the m/EEG inverse problem using accelerated gradient methods. *Physics in medicine and biology*, 57(7):1937, 2012.

[10] S. Kiefer et al. Spectral and angular differential imaging with SPHERE/IFS: Assessing the performance of various PCA-based approaches to psf subtraction. *A&A*, 652:A33, 2021.

[11] D. Mawet et al. Fundamental limitations of high contrast imaging set by small sample statistics. *The Astrophysical Journal*, 792(2):97, 2014.

[12] B. Pairet et al. Mayonnaise: a morphological components analysis pipeline for circumstellar discs and exoplanets imaging in the Near-Infrared. *Monthly Notices of the Royal Astronomical Society*, 503(3):3724–3742, 2021.

[13] R. Soummer et al. Detection and characterization of exoplanets and disks using projections on Karhunen-Loève eigenimages. *The Astrophysical Journal Letters*, 755(2):L28, 2012.

[14] S. Vary et al. Low-rank plus sparse trajectory decomposition for direct exoplanet imaging. In *ICASSP 2023 - 2023 IEEE International Conference on Acoustics, Speech and Signal Processing (ICASSP)*, pages 1–5, 2023.